

Recurrent Auto-Encoders for Enhanced Deep Reinforcement Learning in Wilderness Search and Rescue Planning

Jan-Hendrik Ewers^{a,*}, David Anderson^a, Douglas Thomson^a

^a*Autonomous Systems And Connectivity Research Division, University of Glasgow, Scotland*

Abstract

Wilderness search and rescue operations are often carried out over vast landscapes. The search efforts, however, must be undertaken in minimum time to maximize the chance of survival of the victim. Whilst the advent of cheap multicopters in recent years has changed the way search operations are handled, it has not solved the challenges of the massive areas at hand. The problem therefore is not one of complete coverage, but one of maximizing the information gathered in the limited time available. In this work we propose that a combination of a recurrent autoencoder and deep reinforcement learning is a more efficient solution to the search problem than previous pure deep reinforcement learning or optimisation approaches. The autoencoder training paradigm efficiently maximizes the information throughput of the encoder into its latent space representation which deep reinforcement learning is primed to leverage. Without the overhead of independently solving the problem that the recurrent autoencoder is designed for, it is more efficient in learning the control task. We further implement three additional architectures for a comprehensive comparison of the main proposed architecture. Similarly, we apply both soft actor-critic and proximal policy optimisation to provide an insight into the performance of both in a highly non-linear and complex application with a large observation space. Results show that the proposed architecture is vastly superior to the benchmarks, with soft actor-critic achieving the best performance. This model further outperformed work from the literature whilst having below a fifth of the total learnable parameters and training in a quarter of the time.

1. Introduction

Wilderness search and rescue (WiSAR) missions are some of the most time-sensitive operations in existence. Shaving off seconds in the time to find and the resultant rescue can directly result in saved lives. Over small areas it can be effective to quickly cover the entire search space using modern technology such as drones (Carrell, 2022), however this becomes intractable over larger areas. The search area can quickly balloon into the tens of kilometres in width and depth when considering a WiSAR scenario. This introduces the requirement to take the endurance of the searcher into account as complete coverage is no longer feasible. This is referred to as search planning which aims to maximize a objective given a maximum path length.

Current approaches to using unmanned aerial systems (UAS) during deployment by organisations like Police Scotland Air Support Unit is the pilot-observer model. This mandates that there are always at least two personnel present to operate the UAS no matter the scenario. The pilot flies the drone whilst also

*This work was supported by the Engineering and Physical Sciences Research Council, Grant/Award Number: EP/T517896/1-312561-05

*Corresponding author

Email addresses: j.ewers.1@research.gla.ac.uk (Jan-Hendrik Ewers), david.anderson@glasgow.ac.uk (David Anderson), douglas.thomson@glasgow.ac.uk (Douglas Thomson)

observing and inspecting the live camera feed, whereas the observers is in charge of maintaining a visual line-of-sight to the UAS at all times for safety and legislative reasons. In work by Koester et al. (2004), it was identified that a searcher has a higher probability of detection when not in motion leading to the stop-and-look method. Whilst this work was carried out for foot-based searchers, the same strategy can be observed in Ewers et al. (2023) for UAS pilots. It is therefore evident that the cognitive load of manoeuvring and searching is a key limitation, and that being able to offload the menial flying of the drone frees up the pilot to spend more effort on the search.

Previous work (Ewers et al., 2023, 2025), has shown the strength of Deep Reinforcement Learning (DRL) over analytical and optimal search planning methods. Work by Talha et al. (2022) and Peake et al. (2021) applied DRL to a similar problem, however these algorithms explore the environment during the search and do not have the complete Probability Distribution Map (PDM) at the beginning. This is a reasonable scenario to be in at the start of the search as local area knowledge, maps, and case studies are all available to a pilot before the search begins. Similarly, PDM generation algorithms such as from Hashimoto et al. (2022) are viable solutions to generate the PDM as an input.

The proposed algorithm builds on the previously efforts seen in (Ewers et al., 2025) which had severe limitations due to the policy network architecture. The most major of these limitations was that through the use frame-stacking the maximum number of waypoints in a search path was constrained. Another limitation was the long training time required to train the policy due to its large amount of learnable parameters. This of course also results in poor runtime performance during deployment as multiple gigabytes of memory are consumed to hold the model on potentially resource limited devices.

Mock and Muknahallipatna (2023) found that using frame-stacking over recurrent architectures leads to comparable performance. However, in this formulation the observations from early in the simulation become decreasingly unimportant. In the search planning algorithm from Ewers et al. (2025) this is not the case and every step has an equal impact on the next steps reward. Hence, the policy must be able to observe the observations back to $t = 0$ s to maintain the Markv Decision Process (MDP).

In this work we aim to tackle two of the aforementioned problems: find an alternative to frame-stacking, and increase general performance (training times, model size, overall efficacy). In Raffin et al. (2019) a Auto-Encoder (AE) is successfully used within the DRL loop whilst in (Park et al., 2018) the sequence-to-sequence architecture is introduced for text-based applications. This is the basis to approach the first problem, and also a possible approach to handle the second. We hypothesis that by splitting out the feature extraction phase as a observation preprocessing step we can harness the powerful AE training setup, and thusly reduce the training overhead by not having to learn the feature extraction during the DRL phase. This will then result in two models (AE and DRL policy) working in unison that are specialized and substantially smaller than in Ewers et al. (2025) with better performance.

This work therefore contributes the following advances to the field:

- A framework to decrease training times and to significantly reduce the number of learnable parameter, whilst enhancing final performance through the proposed AE and DRL architecture,
- Empirical evaluation of frame-stacking and recurrent frameworks for large observations,
- Further the discussion in comparing PPO and SAC in a large observation space domain.

Related work is discussed in Section 2. The environmental modelling is presented in Section 3, whilst the RAE and DRL architectures are introduced in Section 4 and Section 5 respectively. Implementation details are outlined in Section 6, followed by results and discussions in Section 7 and Section 8. Finally, a conclusion is drawn in Section 9.

2. Related Work

DRL has seen significant application across exploration planning domains. Zuluaga et al. (2018) focuses on urban scenarios and incorporates frontier exploration into the search task where the agent gathers information on the environment over time. Niroui et al. (2019) uses SLAM with DRL to explore a cluttered

environment, which has many parallels to mining search, in real time. Similarly Peake et al. (2021) applies DRL to WiSAR and employs dual-policy DRL, DDPG and recurrent A2C, which were trained separately to handle the exploration and trajectory planning. Talha et al. (2022) also uses two DRL policies to handle the navigation and exploration separately. These foundational works notably omit consideration of prior probability distributions for target locations. Ewers et al. (2025) explored this scenario and showed that DRL outperforms search planning methods from the literature, however with long training times, and too many parameters to be practical.

One potential solution to reducing the training overhead is to use hierarchical DRL with multiple more specialized models and policies. As previously outlined, Peake et al. (2021) and Talha et al. (2022) apply the dual-policy paradigm but still rely on a single policy to handle the top-level exploration planning. This then implies that the search planning from Ewers et al. (2025) can be coupled with the lower-level trajectory or navigation planning from the aforementioned work. However, the same issues arise in that the mission planning policy is no better than before.

The architecture in Ewers et al. (2025) uses frame-stacking to ensure that the MDP is maintained. This is due to the reward at the current time step being dependent on the position of the agent in all previous time steps. If the agent intersects with the historical path then it is penalized by not gaining any new information. Whilst Mock and Muknahallipatna (2023) found that frame-stacking and recurrent architectures performed similarly, frame-stacking imposes a hard upper limit on the size of the input. The buffer size can be increased to overcome this issue but this has problems of its own. If the buffer is not full during training then inputs associated with data points far in the future cannot be trained leading to inefficient - or even unstable - training. It is therefore imperative to find another approach to handle the temporal input.

In Raffin et al. (2019), the concept of decoupling the feature extraction for DRL is explored. It was found that the proposed method was far superior to the standard single-policy approach in DRL. Interestingly, it was found that this method was only slightly better than an AE. AEs have two components: an encoder applying a transformation on the input into a latent space, followed by a decoder approximating the reverse of this process Berahmand et al. (2024). However, the method from this work requires frame-stacking again to work effectively. Pleines et al. (2022) used a Long-Short Term Memory (LSTM) layer (Hochreiter and Schmidhuber, 1997) within the policy but another approach is to couple this with the aforementioned AE to leverage the sequence-to-sequence architecture proposed in work by Park et al. (2018) to predict the trajectory of a vehicle through a Recurrent Auto-Encoder (RAE). The sequence-to-sequence architecture was also used in Cho et al. (2014) to process complex phrase representations for translations; another domain where there are dependencies on the entire variable length dataset for context.

Proximal Policy Optimisation (PPO) (Schulman et al., 2017), its recurrent variant Recurrent PPO (RPPO) (Raffin et al., 2021; Pleines et al., 2022), and Soft Actor-Critic (SAC) (Haarnoja et al., 2019) are widely used in control problems such as by Kaufmann et al. (2023) and Yue et al. (2022), as well as in other domains such as video gaming (OpenAI, 2019). PPO’s stability and simplicity make it ideal for initial policy convergence in deterministic settings, while SAC’s entropy-driven exploration excels in dynamic environments requiring adaptive action distributions (Shianifar et al., 2025). The contrast between PPO’s bounded policy updates (via advantage function clipping) and SAC’s stochasticity (via the maximum entropy formulation) provides a methodological spectrum to evaluate robustness. PPO has become one of the de facto DRL algorithms in the literature, however Mock and Muknahallipatna (2023) found that it was unable to cope with higher dimensional observation spaces as well as SAC could.

Our work addresses the training instability of frame-stacking through a RAE architecture that compresses temporal dependencies into latent states. By integrating sequence-to-vector trajectory encoding with decoupled feature extraction, we enable dynamic adaptation to environmental uncertainty while maintaining compatibility with the dimensionality constraints of the policy networks. This approach uniquely resolves the conflict between long-horizon probabilistic reasoning and fixed-size observation spaces.

3. Environment Modelling

3.1. Agent Dynamics

The agent within the environment is modelled as a heading control model with a fixed step size sm . It is assumed that any physical vehicle, such as a drone in the case of WiSAR, executing this mission can accurately track the waypoints via its controller or operator. The agent’s state is represented by the 2D position vector $\mathbf{x} = [x, y]^T \in \mathbb{R}^2$ and it’s dynamics are described by the nonlinear system

$$\dot{\mathbf{x}} = s \begin{bmatrix} \cos(\pi(a_t + 1)) \\ \sin(\pi(a_t + 1)) \end{bmatrix} \quad (1)$$

$$\mathbf{y} = \begin{bmatrix} 1 & 0 \\ 0 & 1 \end{bmatrix} \begin{bmatrix} x(t) \\ y(t) \end{bmatrix} \quad (2)$$

where $a_t \in [-1, 1]$ is the agent’s action at time-step t and the Euler integration scheme, $\mathbf{x}_{t+1} = \mathbf{x}_t + \delta t \dot{\mathbf{x}}$, is used with $\delta t = 1s$.

3.2. Probability Distribution Map

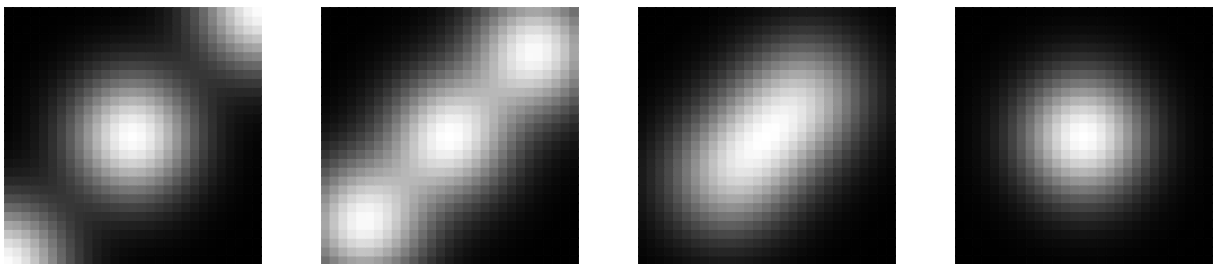
It is assumed that the PDM is known and is modelled as a sum of $N_{gaussian}$ bivariate Gaussians (Ewers et al., 2024). Yao et al. (2017) and Yao et al. (2022) showed that bivariate Gaussians are effective at approximating PDMs. The agent at position \mathbf{x} thus has a probability of being above the true search objective, a missing person for WiSAR, given by

$$p(\mathbf{x}) = \frac{1}{N_{gaussian}} \sum_{i=0}^{N_{gaussian}} \frac{\exp\left\{-\frac{1}{2}(\mathbf{x} - \mu_i)^T \sigma_i^{-1}(\mathbf{x} - \mu_i)\right\}}{\sqrt{4\pi^2 \det\{\sigma_i\}}} \quad (3)$$

where $\mu_i \in \mathbb{R}^2$ and $\sigma_i \in \mathbb{R}^{2 \times 2}$ are the mean location and covariance matrix of the i th bivariate Gaussian respectively. The mean is reset at the start of every episode with

$$\mu_i \sim \mathcal{U}([x_{\min}, x_{\max}], [y_{\min}, y_{\max}]), \forall i \in [0, N_{gaussian}] \quad (4)$$

The covariance is left unchanged to avoid a further tunable simulation parameter. Figure 1 shows how the various PDMs are still highly irregular even with constant covariance due to the randomness introduced by Equation 4.



(a) The three modes are far apart with the saddle being close to 0. (b) The saddle is almost the same value as the maxima of the modes. (c) All three maxima have merged into a pill-shaped area of high value. (d) All maxima are aligned leading to a single hotspot.

Figure 1: Example PDM $p(\mathbf{x})$ with $N_{gaussian} = 3$ and constant covariance. Lighter areas are of higher probability whilst darker ones have lower probability. During search planning the agent would avoid lower probability regions whilst targeting high probability ones to maximize total seen probability.

3.3. Reward Architecture

As the agent moves a constant distance sm every step, it is assumed that the camera follows this path continuously at a fixed height whilst pointing straight down at all times. Therefore, to represent the *seen area* for a given path at time-step t , the path is buffered by $R_{buffer}m$ to give the polygon H_t . All probability from the PDM enclosed within H_t is then *seen* and denoted by p_t . This value, the seen probability, is calculated through

$$I(C) = \oint_C f(\mathbf{x})dC \quad (5)$$

Substituting $C = H_t$ and Equation 3 gives

$$p_t = \oint_{H_t} p(\mathbf{x})dH_t \quad (6)$$

Our goal is to maximize the captured probability mass. To gain insight into how the agent's path affects this, we first focus on the local behaviour of p_t . We analyze the area covered by the agent in two steps, as this provides a foundation for understanding more complex paths. The following lemma demonstrates a crucial property of this two-step area in the simplified case of a uniform PDM.

Lemma 3.1. *For a uniform PDM, $p(\mathbf{x}) = 1$, the area $A(\theta)$ of the region H after two steps, as defined by*

$$A_2(\theta) = \overbrace{4sR_{buffer}}^{\text{Main Area}} + \overbrace{\pi R_{buffer}^2}^{\text{Semi-Circle}} + \overbrace{\frac{1}{2}R_{buffer}^2\theta}^{\text{Rounded corner } g(\theta)} - \overbrace{R_{buffer}^2 \tan\left(\frac{\theta}{2}\right)}^{\text{Overlap } f(\theta)} \quad (7)$$

$$\forall \theta \in \left[0, 2 \arctan\left(\frac{s}{R_{buffer}}\right)\right]$$

where R_{buffer} and s are constants, is maximized when $\theta = 0$.

Proof. Assume, for the sake of contradiction, that there exists a $\theta^* \in \left[0, 2 \arctan\left(\frac{s}{R_{buffer}}\right)\right]$ such that $A_2(\theta^*) > A_2(0)$. The derivative of A_2 with respect to θ is

$$\frac{dA_2}{d\theta} = \frac{1}{2}R_{buffer}^2 \left(1 - \sec^2\left(\frac{\theta}{2}\right)\right) \quad (8)$$

Since $1 - \sec^2(x) \leq 0 \forall x \in \mathbb{R}$, we have $\frac{dA_2}{d\theta} \leq 0 \forall \theta \in \left[0, 2 \arctan\left(\frac{s}{R_{buffer}}\right)\right]$. Because the derivative is non-positive, $A_2(\theta)$ is a monotonically decreasing function on the given interval. Since $A_2(\theta)$ is monotonically decreasing, for any $\theta^* > 0$, it must be the case that $A_2(\theta^*) \leq A_2(0)$. Our assumption that there exists a θ^* such that $A_2(\theta^*) > A_2(0)$ must be false. Therefore, the maximum value of $A_2(\theta)$ is achieved when $\theta = 0$. \square

Further insights can be garnered by applying Green's theorem

$$\oint_C (Ldx + Mdy) = \iint_D \left(\frac{\partial M}{\partial x} - \frac{\partial L}{\partial y}\right)dA \quad (9)$$

with $\frac{\partial M}{\partial x} - \frac{\partial L}{\partial y} = 1$. This shows that decreasing the boundary $C = H_2$ reduces the area of the region D bounded by C . With a uniform PDM, maximizing the geometric area is equivalent to maximizing the captured probability mass. From Theorem 3.1, the buffered polygon formulation maximizes the integral when $\theta = 0$ for a uniform PDF. However, if $\frac{\partial M}{\partial x} - \frac{\partial L}{\partial y}$ is not constant it could be beneficial to increase θ and therefore reducing the area in order to maximize the encapsulated values.

Special consideration must be taken for the case where $\frac{s}{R_{buffer}} < \frac{\pi}{2}$ as Theorem 3.1 does not hold and must be further explored. This constraint, however, is always met in this work.

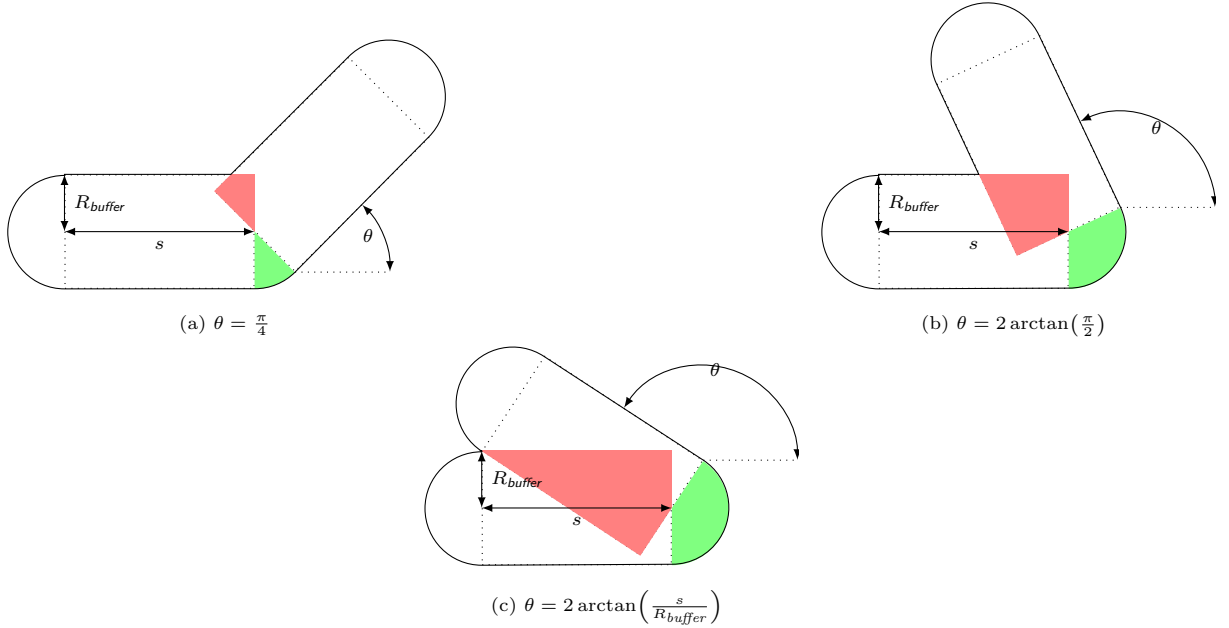


Figure 2: Visualizing H_2 (H_t after two steps) with different θ . The areas coloured in red and green represent $f(\theta)$ and $g(\theta)$ from Equation 7 respectively.

The action is correlated to the reward by considering the change in accumulated probability at time t , defined as

$$\Delta p_t = p_t - p_{t-1} \quad (10)$$

To normalize this change in accumulated probability we introduce the scaling constants k and p_A . Constant k relates the area of a single isolated step to the total search area, $A_{\text{area}} \text{m}^2$. Simplifying Equation 7 to the single step case using the constants defined in Figure 2, gives the ratio

$$k = \frac{A_{\text{area}}}{R_{\text{buffer}}(\pi R_{\text{buffer}} + 2s)} \quad (11)$$

Constant p_A is the total probability enclosed within the total search area given by substituting $H_t = A$ in Equation 6. This gives the scaled probability efficiency reward

$$r = \frac{k}{p_A} \Delta p_t \quad (12)$$

The ratio of change in accumulated probability to total probability enclosed within the search area satisfies the constraint that $0 \leq \frac{\Delta p_t}{p_A} \leq 1$. This ratio is the probability efficiency, $e_{p,t}$, and provides a useful insight into the performance of a given path.

Further reward shaping is applied to discourage future out-of-bounds actions (w_{oob}), and to penalize visiting areas of very low probability (w_0). The augmented reward r' is given by

$$r' = \begin{cases} -w_{oob}, & \mathbf{x}_t \notin [x_{\min}, x_{\max}] \times [y_{\min}, y_{\max}] \\ w_r r, & \Delta p_t > \epsilon \\ -w_0, & \text{else} \end{cases} \quad (13)$$

3.4. Observation Processing

The observation vector at time t is denoted by s_t . To ensure flexibility when designing the architectures, the available sub-states are given in Table 1 with architecture-specific observation space definitions given in Section 5.

Table 1: Definition of the five state observations

Sub-state	Symbol	Definition
Path	s_{path}	$(\mathbf{x} \parallel 0^{2 \times N_{\text{waypoints}} - t})^T$
PDM	s_{PDM}	$[\mu_0, \sigma_0, \dots, \mu_G, \sigma_G]^T$
Position	s_{pos}	\mathbf{x}_t
Out-of-bounds	s_{oob}	$\mathbf{x}_t \in [x_{\min}, x_{\max}] \times [y_{\min}, y_{\max}]$
Number of steps	s_{steps}	t

4. Recurrent Autoencoder

Recurrent encoders project a multidimensional input sequence to a fixed-length latent space z_t through $E_\phi(x_t) \mapsto z_t$, parametrized by ϕ (Cho et al., 2014). This work this uses the LSTM architecture (Hochreiter and Schmidhuber, 1997). LSTM networks have a hidden state h_t that is passed through the layers which holds the memory of previously seen states whereas c_t is similar in that it carries the information about the sequence over time but is unique to each cell. Both h_t and c_t are critical to the handling of sequential data. For each element in the input sequence, each layer computes the function

$$\begin{aligned}
 i_t &= \sigma(W_{xi}x_t + W_{hi}h_{t-1} + b_i) \\
 f_t &= \sigma(W_{xf}x_t + W_{hf}h_{t-1} + b_f) \\
 g_t &= \tanh(W_{xg}x_t + W_{hg}h_{t-1} + b_g) \\
 o_t &= \sigma(W_{xo}x_t + W_{ho}h_{t-1} + b_o) \\
 c_t &= f_t \odot c_{t-1} + i_t \odot g_t \\
 h_t &= o_t \odot \tanh(c_t)
 \end{aligned} \tag{14}$$

where i_t , f_t , g_t , and o_t are the input, forget, cell, and output gates respectively, σ is the sigmoid function, \odot is the hadamard product, and W and b are the parameter matrices and vectors. h_{t-1} is the hidden state of the previous layer at time $t-1$ and is initialized at time $t=0$ to be zero. The LSTM unit internal structure can be seen in Figure 3 showing the three gates interacting with the various states. y_t is the output and is equal to h_t of the final layer if multiple layers are used.

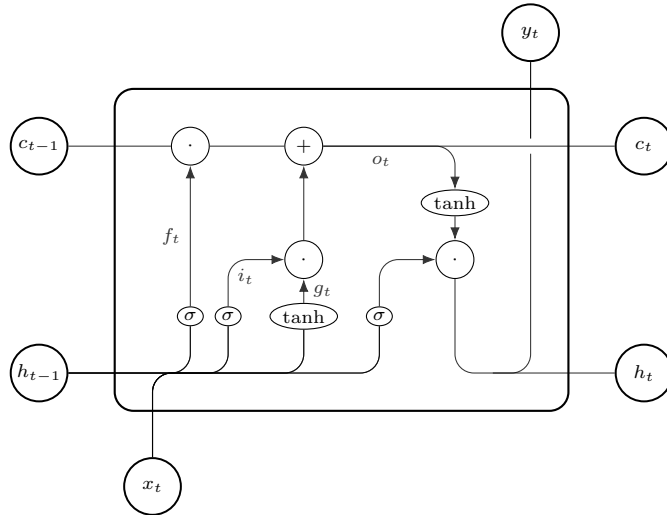


Figure 3: The Long Short-Term Memory unit internal structure from Equation 14

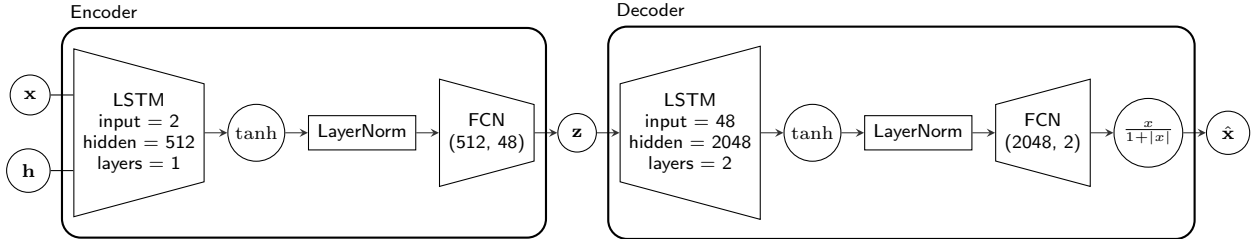


Figure 4: RAE architecture using LSTMs for encoding and decoding. Using an unbalanced architecture, with the decoder being larger than the encoder, enables higher quality reconstruction which results in faster training and better performance. Softsign is applied to the decoder output to ensure that values meet the $s_{\text{path}} \in [-1, 1]$ requirement whilst providing close to linear mappings in this range.

An approximation of the input is then made by the decoder D_θ , parameterized by θ , of the same length. The decoder is passed the latent space z_t as many times as there are rows in x_t , as well as the hidden state h_t and cell state c_t . Each output is then the estimated value of the corresponding item in the input sequence. The loss is calculated using the mean square error

$$\mathcal{L}(s, \hat{s}, z) = \frac{1}{\dim(s)} \sum_{i=1}^N (\hat{s}_i - s_i)^2 \quad (15)$$

The optimal RAE for s_{path} encoding is then found by

$$\phi^*, \theta^* = \arg \min_{\phi, \theta} \mathcal{L}[s_{\text{path}}, D_\theta(E_\phi(s_{\text{path}})), E_\phi(s_{\text{path}})] \quad (16)$$

The RAE network can be seen in Figure 4. Using an unbalanced setup in favour of the decoder gives a higher reconstruction potential, which leads to better encoder training. The larger decoder compensates for any loss of information during encoding, ensuring that even a suboptimal latent representation can still result in high-quality training updates. This setup also stabilizes training and accelerates convergence by allowing the decoder’s higher capacity to handle complex reconstruction tasks effectively.

5. Model Architectures

The principal architecture introduced in this work is the Long Short-Term Memory AE with Soft Actor-Critic (LSTMAE_SAC). This model leverages a RAE, specifically an LSTM-based AE as previously defined in Section 4, to handle path history feature extraction. The LSTMAE is coupled with the SAC algorithm, which has demonstrated robust performance in continuous action spaces with large observation spaces. The LSTMAE_SAC architecture is designed to efficiently process temporal information from the agent’s path history, potentially reducing the need for an extremely large network as observed in previous work (Ewers et al., 2025).

To comprehensively evaluate the efficacy of LSTMAE_SAC, a suite of comparative architectures were developed. These vary in their DRL algorithms, path observation augmentation techniques, and inner-model feature extraction methods. The key variants are defined in Table 2 and were designed to systematically explore the impact of different components:

- Efficacy of path observation augmentation,
- Differences in DRL algorithm,
- Impact on inner-model feature extraction in lue of path observation augmentation.

Table 2: Definitions of architectures

Architecture title	RL Algorithm	Path Observation Augmentation	Inner-model Feature Extraction	Observation Space
LSTMAE_SAC	SAC	LSTM-AE	None	$(z_{\text{path}}, s_{\text{PDM}})$
LSTMAE_PPO	PPO	LSTM-AE	None	$(z_{\text{path}}, s_{\text{PDM}})$
LSTM_PPO	RPPO	None	None	$(s_{\text{pos}}, s_{\text{PDM}})$
FS_SAC_LSTM	SAC	Frame Stacking	LSTM	$(s_{\text{path}}, s_{\text{PDM}})$
FS_SAC_FCEN	SAC	Frame Stacking	Fully Connected Network	$(s_{\text{path}}, s_{\text{PDM}})$
FS_SAC_CONV2D	SAC	Frame Stacking	2D Convolution	$(s_{\text{path}}, s_{\text{PDM}})$
FS_PPO_LSTM	PPO	Frame Stacking	LSTM	$(s_{\text{path}}, s_{\text{PDM}})$
FS_PPO_FCEN	PPO	Frame Stacking	Fully Connected Network	$(s_{\text{path}}, s_{\text{PDM}})$
FS_PPO_CONV2D	PPO	Frame Stacking	2D Convolution	$(s_{\text{path}}, s_{\text{PDM}})$

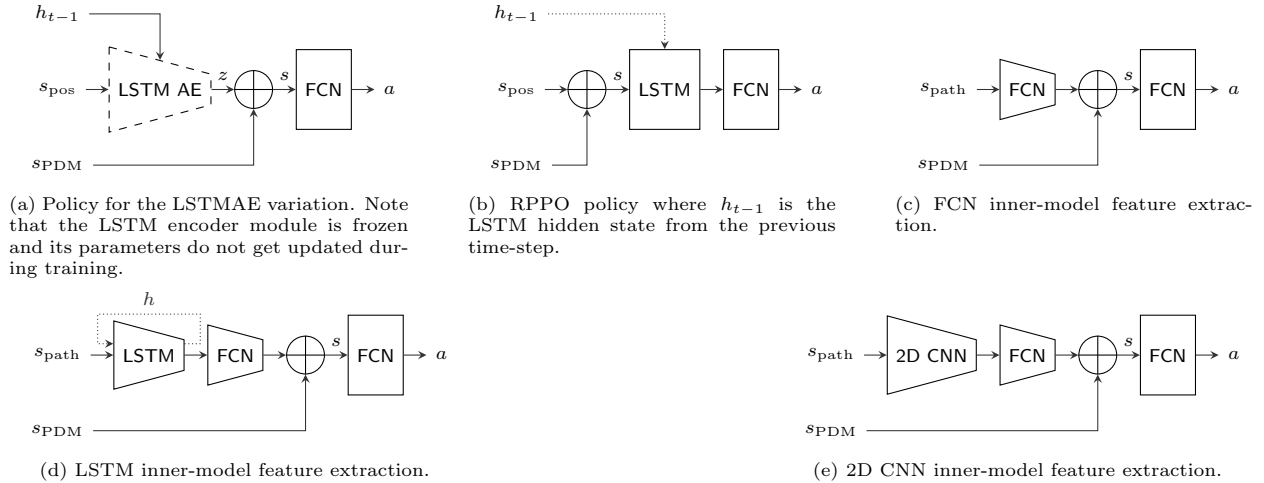


Figure 5: The five proposed policy architectures for use with either PPO, RPPO, or SAC. Figure (b) is only used with RPPO.

6. Practical Implementation Details

6.1. Cubature

The integral is calculated using a cubature integration scheme (Cools et al., 1997) with constrained Delaunay triangulation (Chew, 1987) to subdivide H_t into triangles for fast computation. The use of pseudo-continuous over discrete integration has shown to greatly reduce noise in previous work (Ewers et al., 2024). Whilst noise can be beneficial to promote exploration, this must be controllable and tunable. Reducing noise in the reward function, where cubature is being used, is critical to maximize learning efficiency else expensive techniques have to be employed (Wang et al., 2020).

6.1.1. Recurrent Encoder

Training. During training the test dataset was unbatched and chunked into $N \sim \mathcal{U}(2, k)$ length sections where k is the length of the longest path in the batch. If $N < k$ then the hidden states would be reused for the next section rather than resetting. This significantly improved the speed of convergence. Automatic mixed precision was used to further increase training times. A no-improvement criterion was used where training would terminate if the amount of epochs since a loss function decrease breaches a patience threshold.

Deployment. The recurrent encoder, as detailed in Section 4, undergoes separate training from the DRL models with its parameters frozen during DRL training. This isolation prevents latent space divergence that could destabilize the learning during online updates. In our implementation, the encoder resides in the observation preprocessing pipeline rather than the policy network itself. This architectural choice minimizes replay buffer memory and compute requirements during training (critical for SAC’s experience replay mechanism), though deployment permits alternative configurations. The two viable deployment strategies are:

- **Hidden State Propagation:** Stores only the encoder’s hidden states (including cell state), giving a constant runtime performance per step with fixed memory usage (hidden states).
- **Full History Processing:** Maintains complete trajectory histories, with the memory requirements and runtime performance growing linearly with the episode length.

In this work the former approach - hidden state propagation - is used. The full history processing approach would be required for other techniques such as temporal convolution networks (Lea et al., 2016) or transformers (Vaswani et al., 2017).

6.2. Further Architecture Details

The RPPO implementation used in this work is from Raffin et al. (2021) which aligns closely with Pleines et al. (2022). The 2D convolution kernel inner-model feature extractor for FS_PPO_CONV2D and FS_SAC_CONV2D is from Mnih et al. (2015)

7. Results

7.1. Experimental setup

Each model was trained over 1.000E7 step with 8 workers on a local Ubuntu 22.04 machine with a AMD Ryzen 9 5950X CPU with a NVIDIA RTX A6000 GPU and 64GB of RAM. Runs terminated when invalid training updates were attempted which only happened during periods of extremely poor performance. At least five runs per architecture were undertaken with randomized starting seeds which aligns with the best practices outlined in work by Agarwal et al. (2022) to ensure robust analysis for DRL results. The set of run configurations was generated and then randomized during training to avoid any possibility of unforeseen interactions.

The RAE training dataset contained 5E4 unique paths which were generated using LHC_GW_CONV (Lin and Goodrich, 2009) with the same parameters as in this work. The recurrent encoder was trained once and then deployed for all following runs.

7.2. Evaluation Metrics

This section outlines the metrics used to evaluate the performance of the different architectures.

7.2.1. Mean Step Reward

The average reward received by the agent at each time step during an episode. A higher mean step reward indicates that the agent is making more effective decisions that lead to higher rewards at each step.

7.2.2. Mean Rollout Episode Reward

The average reward accumulated by the agent over a complete episode during the rollout phase. This metric reflects the overall performance of the learned policy in generating high-quality paths.

7.2.3. Mean Episode Length

The average number of time steps taken by the agent before the episode terminates. A longer mean episode length generally indicates that the agent is able to explore the environment more effectively and find longer, more efficient paths.

7.2.4. Maximum Probability Efficiency

The highest achieved probability of reaching the target within a given search area observed during training as defined in Section 3.3. This metric directly reflects the search efficacy of the architecture, indicating how well it can find the target within the specified search space.

7.2.5. Runtime

The total time or steps taken by the architecture to train. This metric is crucial for practical applications, as it indicates the computational cost of training the architecture.

7.2.6. Mean Probability Efficiency

Similar to the maximum probability efficiency, it is the mean probability efficiency achieved during evaluation. This metric provides a comprehensive assessment of the architecture’s search performance across multiple runs.

7.2.7. Number of Parameters

The total number of learnable parameters in the neural network architecture. This metric provides an indication of the model’s complexity and computational requirements.

7.3. Architecture

From Figure 6 it is clear that LSTMAE_SAC, LSTMAE_PPO, LSTM_PPO, and FS_PPO_CONV2D had the best rollout reward performance with very stable learning curves. However, the FS_SAC_CONV2D variant was by far the least stable and consistently crashed during training with illegal update steps. This is further corroborated by Table 3 with FS_PPO_CONV2D having one of the highest mean runtime steps at 9.820E6 and FS_SAC_CONV2D having the lowest at 1.000E6.

Table 3: Aggregated architecture results over multiple metrics gathered at the end of a training run.

Architecture	Mean Step Reward		Mean Episode Length		Maximum Probability Efficiency		Runtime [s/.00010 ³]		Runtime [steps/.00010 ⁶]	
	Mean.	Std.	Mean.	Std.	Mean.	Std.	Mean.	Std.	Mean.	Std.
FS_PPO_CONV2D	3.290	5.190	3.690	1.190	1.020	1.880	51.100	7.710	9.820	0.682
FS_PPO_FCN	2.720	9.370	2.160	1.080	6.590	1.240	45.800	15.400	9.360	1.670
FS_PPO_LSTM	2.730	1.150	1.640	7.390	4.370	8.880	94.800	24.900	9.870	0.591
FS_SAC_CONV2D	2.260	1.030	1.010	1.630	3.630	2.950	9.770	4.550	1.000	0.316
FS_SAC_FCN	2.070	9.770	2.210	1.920	7.900	2.500	79.900	52.700	7.230	3.720
FS_SAC_LSTM	1.360	1.140	3.200	2.510	8.430	1.670	280.000	125.000	7.100	2.990
LSTMAE_PPO	5.200	6.100	5.110	4.250	1.760	6.710	156.000	49.900	10.000	0.000
LSTMAE_SAC	5.370	4.310	5.730	6.090	1.920	1.160	255.000	55.100	9.750	0.610
LSTM_PPO	4.130	5.120	5.540	7.400	1.640	1.950	355.000	128.000	8.260	3.120

With the simulation terminating prematurely if the agent steps out-of-bounds, it is important for the mean episode length to be as close to the maximum simulation length as possible. The worst performance was again FS_SAC_CONV2D with 1.010E1 showing a complete lack of generalization. LSTMAE_SAC had the highest mean episode length at 5.730E1 with LSTMAE_PPO and LSTM_PPO achieving similar results at 5.110E1 and 5.540E1 respectively. None of the frame-stacking variants were able to breach the 4.000E1 barrier with FS_SAC_CONV2D coming closest at 3.690E1 which aligns with the performance displayed in Figure 6.

Mean step reward and maximum probability efficiency should strongly correlate from the definition of reward in Equation 13. However, the latter is the key metric as it directly relates to the search efficacy. Similar to previous metrics, FS_SAC_CONV2D displayed the poorest performance with a score of

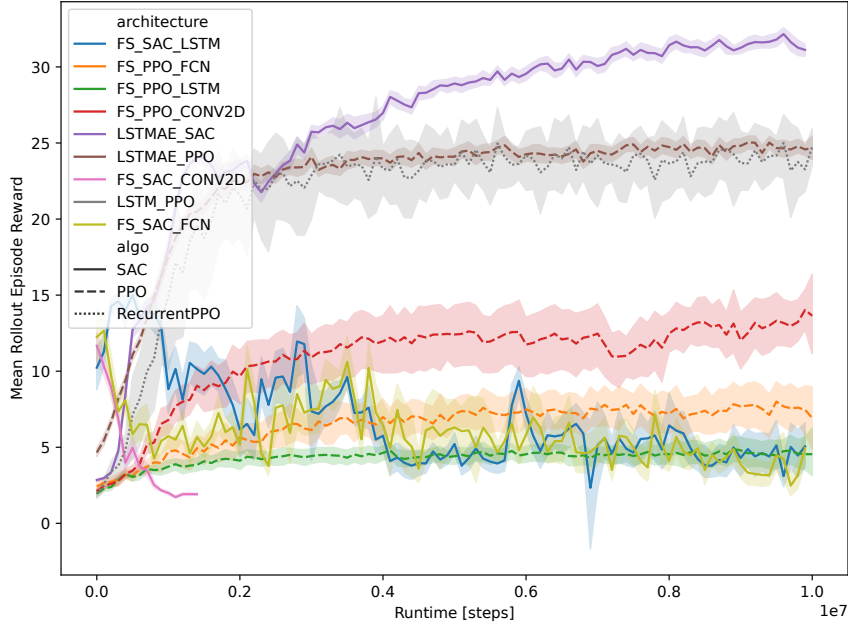


Figure 6: Mean rollout episode reward over global step for all architectures highlighting the training stability provided by the LSTMAE.

$3.630\text{E}-2$. FS_PPO_CONV2D, again, was the best of the frame-stacking variants with a score of $1.020\text{E}-1$. LSTMAE_PPO and LSTM_PPO also performed inline with previous results with $1.760\text{E}-1$ and $1.640\text{E}-1$ respectively. Whilst LSTMAE_PPO has a higher mean maximum probability efficiency, it also has a lower standard deviation of $6.710\text{E}-3$ compared to $1.950\text{E}-2$ across more runs. This could indicate the additional stability offered by having a static LSTMAE compared to the internalized LSTM module of LSTM_PPO from Figure 5b. Furthermore, this could hint at the vanishing gradient problem that recurrent networks suffer from.

Ultimately, LSTMAE_SAC showed the best performance across mean step reward ($1.700\text{E}-2$ higher than LSTMAE_PPO), mean episode length ($1.900\text{E}-2$ higher than LSTM_PPO), and maximum probability efficiency with a value of $1.920\text{E}-1$ ($1.600\text{E}-2$ higher than LSTMAE_PPO). Contrary to the runtime results from Table 3, Figure 6 shows a training curve that had not reached its maxima whilst starkly outperforming the competing variants.

7.4. Ablation Study: Reinforcement Algorithm

SAC and PPO have been extensively compared in the literature, however, it is typically only the environment that is being changed. In this comparison the result from the various architectures are grouped by DRL algorithm with a consistent environment and hyperparameters. This will give an indication of the robustness and sensitivity to network changes.

Figure 6 displays the inter-quartile range of the maximum probability efficiency from Table 3. This shows that neither PPO nor SAC have a clear advantage for the frame-stacking variant. However, the LSTMAE results clearly show that SAC outperforms PPO here. The aggregated mean for PPO is $1.430\text{E}-1$ compared to $1.370\text{E}-1$ for SAC showing that PPO perhaps has a slight edge. However, applying a p-test gives a p-value of 0.61 which implies that the results are not conclusive.

Isolating the top frame-stacking (FS_PPO_CONV2D and FS_SAC_LSTM) architectures results in a different outcome. SAC has a higher aggregated mean maximum probability efficiency of $1.540\text{E}-1$ whilst PPO only achieves $1.430\text{E}-1$. A p-test, however, also reveals that the the results are not conclusive with a p-value of 0.48.

Table 4: Aggregated algorithm (PPO, RPPO, SAC) results over multiple metrics gathered at the end of a training run.

Algorithm	Mean Step Reward		Mean Episode Length		Maximum Probability Efficiency		Runtime [s/.00010 ³]		Runtime [steps/.00010 ⁶]	
	Mean	Std.	Mean	Std.	Mean	Std.	Mean	Std.	Mean	Std.
PPO	3.530	1.340	3.170	1.650	9.820	5.400	90.800	53.800	9.780	0.905
SAC	3.140	1.900	3.420	2.360	1.120	6.570	167.000	129.000	6.890	3.850
RPPO	4.130	5.120	5.540	7.400	1.640	1.950	355.000	128.000	8.260	3.120

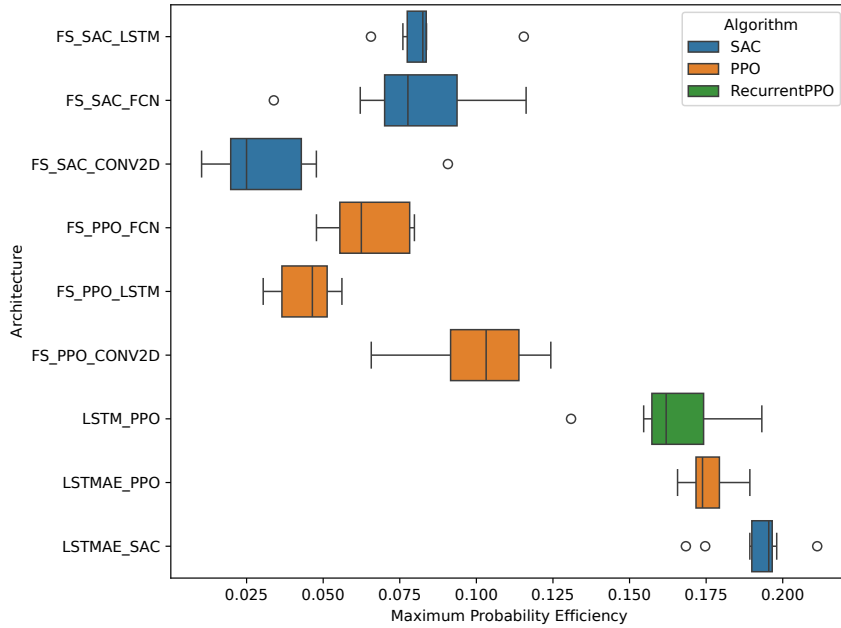


Figure 7: Maximum probability efficiency during training for all architecture variants with colour coded by DRL algorithm.

7.5. Ablation Study: Path Feature Extraction

The main contribution of this work is the use of the LSTMAE to handle the feature extraction. It is therefore imperative to evaluate its efficacy compared to the much simpler frame-stacking. Table 5 shows the aggregated performance of the various feature extractors which closely align to those from Section 7.3. LSTMAE_* is the most performant path feature extraction methods across all key performance metrics. All frame-stacking variants have low mean episodes lengths and low mean step reward. Most importantly, the mean maximum probability efficiency for the best frame-stacking variant, FS_*_CONV2D, is less than half as performant as LSTMAE_*.

As expected from Section 7.4, LSTMAE_* also outperforms LSTM_* in all metrics from Table 5. This further highlights the efficiency of the RAE to capture the relevant information before DRL training to allow the DRL policy to focus on control.

Table 5: Aggregated path feature extraction results over multiple metrics gathered at the end of a training run.

Path Feature Extraction	Mean Step Reward		Mean Episode Length		Maximum Probability Efficiency	
	Mean	Std.	Mean	Std.	Mean	Std.
FS_*_CONV2D	2.880	8.960	2.620	1.630	7.600	4.050
FS_*_FCN	2.420	9.840	2.180	1.480	7.200	1.990
FS_*_LSTM	2.250	1.300	2.190	1.710	5.800	2.320
LSTMAE_*	5.540	6.520	5.620	6.500	2.010	3.040
LSTM_*	4.130	5.120	5.540	7.400	1.640	1.950

7.6. Benchmark

Previous work has shown that FS_SAC_FCNC with a large enough network can outperform optimisation-based algorithms from the literature in (Ewers et al., 2025). A key limitation of this approach was the large number of parameters and long training times required to achieve these results. The results from Section 7.3 were achieved using a core policy of dimensions 2×256 whereas (Ewers et al., 2025) used 8×2000 . For a fairer comparison, a 2×2000 version of LSTMAE_SAC was also trained.

Table 6 shows the mean probability efficiency from 2000 generated paths. It is evident that the smaller variants of both FS_SAC_FCNC and LSTMAE_SAC performed poorer than their larger counterparts. However, the smaller LSTMAE_SAC is only worse than the large FS_SAC_FCNC by a margin of $2.400E-2$ whilst having 0.27% the number of learnable parameters. Large LSTMAE_SAC, which has 14.0% of the amount of learnable parameters of large FS_SAC_FCNC, clearly outperforms all others variants. A performance difference of $4.000E2$ might hint at a insignificant result, however the sample sizes were above 2000 resulting in a p-value of 0.0151 which is above the threshold of 0.05 showing a meaningful difference in distributions. Large LSTMAE_SAC therefore outperforms large FS_SAC_FCNC whilst being only 14% of the size and only needing to be trained for 23% of the time (90 days for Ewers et al. (2025)) and 21 days for large LSTMAE_SAC before it reached the no-improvement termination criterion).

8. Discussion

These results demonstrate the effectiveness of the proposed LSTMAE_SAC architecture for search planning. The LSTMAE effectively captures temporal dependencies within the path, leading to improved performance and stability compared to simpler frame-stacking methods. The RAE training harness maximizes the information throughput in the latent representation which is akin to lossy compression. This prevents the onus from being on the DRL algorithm to perform the same function. Furthermore, the recurrent network allows maximum throughput regardless of path length - from 2 steps to N - since every neuron within

Table 6: Mean probability efficiency from over 2000 generated paths by the respective architectures.

Architecture	Mean	Std.	Core Policy	# Parameters
LSTMAE_SAC	2.000E−1	5.700E−2	2×2000	2.170E7
LSTMAE_SAC	1.720E−1	6.170E−2	2×256	4.250E5
FS_SAC_FCIN (Ewers et al., 2025)	1.960E−1	4.710E−2	8×2000	1.550E8
FS_SAC_FCIN	9.030E−3	1.910E−2	2×256	4.360E5
LHC_GW_CONV (Lin and Goodrich, 2009)	1.210E−1	8.020E−2	n/a	n/a

the policy is trainable regardless of state. The training stability seen in Figure 6 underlines this with both LSTMAE_PPO and LSTMAE_SAC having stable learning curves.

While further investigation is needed to definitively determine the optimal DRL algorithm over all architectures, the results show that SAC has an edge over PPO when used with LSTMAE. This aligns with results from Mock and Muknahallipatna (2023) which suggested that SAC is better for larger dimensional observation spaces.

Isolating the path feature extraction from the DRL algorithm in Section 7.4 suggested that the frame-stacking with LSTM was the poorest performer with LSTMAE being the best. This further provides evidence to the theory that the RAE is superior to standalone DRL. On the other hand, LSTM_PPO is close in performance to LSTMAE_PPO which suggests that simple frame-stacking is the main issues.

The significant performance improvement of the larger LSTMAE_SAC over the larger FS_SAC_FCIN in Section 7.6 highlights the true efficiency and potential of the proposed approach. Similarly, the minor performance difference between large FS_SAC_FCIN and small LSTMAE_SAC shows the power of the highly specialized network architecture proposed in this work. This suggests that the LSTMAE_SAC in general can achieve high performance with fewer parameters and shorter training times, making it a promising approach for real-world applications where computational budgets can be limited.

9. Conclusion

In this study, we have presented a novel approach to enhancing WiSAR missions through the integration of an LSTM-based RAE with DRL. The challenges associated with traditional search planning methods, particularly in large and complex environments, necessitate solutions that can optimize both efficiency and effectiveness in locating missing persons.

Our proposed framework addresses key limitations of existing methodologies by decoupling feature extraction from the policy training phase, thereby significantly reducing the number of learnable parameters and improving training speeds. By employing a RAE architecture, we have demonstrated that it is possible to maintain high performance while also ensuring the model is lightweight enough for deployment on resource-constrained devices. The empirical results indicate that our approach enhances the probability of detection and thus accelerates the overall search process, which is critical in time-sensitive rescue scenarios.

Furthermore, this work contributes to the growing body of literature on DRL applications in search planning by providing a comprehensive evaluation of various architectures, including comparisons between PPO and SAC algorithms in large observation domains. SAC outperformed PPO for the proposed architecture whereas PPO and SAC were similar for the rest. However, FS_PPO_CONV2D was the best non-recurrent architecture whilst FS_SAC_CONV2D was the worst showing that this result is application specific. These findings underscore that DRL is not a golden bullet and the importance of careful model engineering when tackling difficult problems.

References

Agarwal, R., Schwarzer, M., Castro, P. S., Courville, A., and Bellemare, M. G. (2022). Deep Reinforcement Learning at the Edge of the Statistical Precipice.

- Berahmand, K., Daneshfar, F., Salehi, E. S., Li, Y., and Xu, Y. (2024). Autoencoders and their applications in machine learning: A survey. *Artificial Intelligence Review*, 57(2):28.
- Carrell, S. (2022). Flying to the rescue: Scottish mountain teams are turning to drones. *The Guardian*.
- Chew, L. P. (1987). Constrained delaunay triangulations. *Algorithmica*, 4(1-4):97–108.
- Cho, K., van Merriënboer, B., Gulcehre, C., Bahdanau, D., Bougares, F., Schwenk, H., and Bengio, Y. (2014). Learning Phrase Representations using RNN Encoder-Decoder for Statistical Machine Translation.
- Cools, R., Pluym, L., and Laurie, D. (1997). Algorithm 764: Cubpack++: A C++ package for automatic two-dimensional cubature. *ACM Transactions on Mathematical Software*, 23(1):1–15.
- Ewers, J.-H., Anderson, D., and Thomson, D. (2023). Optimal path planning using psychological profiling in drone-assisted missing person search. *Advanced Control for Applications*, page e167.
- Ewers, J.-H., Anderson, D., and Thomson, D. (2025). Deep reinforcement learning for time-critical wilderness search and rescue using drones. *Frontiers in Robotics and AI*, 11:1527095.
- Ewers, J.-H., Swinton, S., Anderson, D., McGookin, E., and Thomson, D. (2024). Enhancing Reinforcement Learning in Sensor Fusion: A Comparative Analysis of Cubature and Sampling-based Integration Methods for Rover Search Planning. In *2024 IEEE/RSJ International Conference on Intelligent Robots and Systems (IROS)*, pages 7825–7830, Abu Dhabi, United Arab Emirates. IEEE.
- Haarhoja, T., Zhou, A., Hartikainen, K., Tucker, G., Ha, S., Tan, J., Kumar, V., Zhu, H., Gupta, A., Abbeel, P., and Levine, S. (2019). Soft Actor-Critic Algorithms and Applications.
- Hashimoto, A., Heintzman, L., Koester, R., and Abaid, N. (2022). An agent-based model reveals lost person behavior based on data from wilderness search and rescue. *Scientific Reports*, 12(1):5873.
- Hochreiter, S. and Schmidhuber, J. (1997). Long Short-Term Memory. *Neural Comput.*, 9(8):1735–1780.
- Kaufmann, E., Bauersfeld, L., Loquercio, A., Müller, M., Koltun, V., and Scaramuzza, D. (2023). Champion-level drone racing using deep reinforcement learning. *Nature*, 620(7976):982–987.
- Koester, R., Cooper, D. C., Frost, J. R., and Robe, R. Q. (2004). Sweep Width Estimation for Ground Search and Rescue. *undefined*.
- Lea, C., Vidal, R., Reiter, A., and Hager, G. D. (2016). Temporal Convolutional Networks: A Unified Approach to Action Segmentation.
- Lin, L. and Goodrich, M. A. (2009). UAV intelligent path planning for wilderness search and rescue. *2009 IEEE/RSJ International Conference on Intelligent Robots and Systems, IROS 2009*, 0(1):709–714.
- Mnih, V., Kavukcuoglu, K., Silver, D., Rusu, A. A., Veness, J., Bellemare, M. G., Graves, A., Riedmiller, M., Fidjeland, A. K., Ostrovski, G., Petersen, S., Beattie, C., Sadik, A., Antonoglou, I., King, H., Kumaran, D., Wierstra, D., Legg, S., and Hassabis, D. (2015). Human-level control through deep reinforcement learning. *Nature*, 518(7540):529–533.
- Mock, J. W. and Muknahallipatna, S. S. (2023). A Comparison of PPO, TD3 and SAC Reinforcement Algorithms for Quadruped Walking Gait Generation. *Journal of Intelligent Learning Systems and Applications*, 15(1):36–56.
- Niroui, F., Zhang, K., Kashino, Z., and Nejat, G. (2019). Deep Reinforcement Learning Robot for Search and Rescue Applications: Exploration in Unknown Cluttered Environments. *IEEE Robotics and Automation Letters*, 4(2):610–617.
- OpenAI (2019). Dota 2 with Large Scale Deep Reinforcement Learning. *arXiv:1912.06680 [cs]*.
- Park, S. H., Kim, B., Kang, C. M., Chung, C. C., and Choi, J. W. (2018). Sequence-to-Sequence Prediction of Vehicle Trajectory via LSTM Encoder-Decoder Architecture. In *2018 IEEE Intelligent Vehicles Symposium (IV)*, pages 1672–1678.
- Peake, A., McCalmon, J., Zhang, Y., Myers, D., Alqahtani, S., and Pauca, P. (2021). Deep Reinforcement Learning for Adaptive Exploration of Unknown Environments. In *2021 International Conference on Unmanned Aircraft Systems (ICUAS)*, pages 265–274.
- Plaines, M., Pallasch, M., Zimmer, F., and Preuss, M. (2022). Generalization, Mayhems and Limits in Recurrent Proximal Policy Optimization.
- Raffin, A., Hill, A., Gleave, A., Kanervisto, A., Ernestus, M., and Dormann, N. (2021). Stable-Baselines3: Reliable Reinforcement Learning Implementations. *Journal of Machine Learning Research*, (22).
- Raffin, A., Hill, A., Traoré, R., Lesort, T., Díaz-Rodríguez, N., and Filliat, D. (2019). Decoupling feature extraction from policy learning: Assessing benefits of state representation learning in goal based robotics. <https://arxiv.org/abs/1901.08651v3>.
- Schulman, J., Wolski, F., Dhariwal, P., Radford, A., and Klimov, O. (2017). Proximal Policy Optimization Algorithms.
- Shianifar, J., Schukat, M., and Mason, K. (2025). Optimizing Deep Reinforcement Learning for Adaptive Robotic Arm Control. In González-Briones, A., Julian Inglada, V., El Bolock, A., Marco-Detchart, C., Jordan, J., Mason, K., Lopes, F., and Sharaf, N., editors, *Highlights in Practical Applications of Agents, Multi-Agent Systems, and Digital Twins: The PAAMS Collection*, volume 2149, pages 293–304. Springer Nature Switzerland, Cham.
- Talha, M., Hussein, A., and Hossny, M. (2022). Autonomous UAV Navigation in Wilderness Search-and-Rescue Operations Using Deep Reinforcement Learning. In Aziz, H., Corrêa, D., and French, T., editors, *AI 2022: Advances in Artificial Intelligence*, Lecture Notes in Computer Science, pages 733–746, Cham. Springer International Publishing.
- Vaswani, A., Shazeer, N., Parmar, N., Uszkoreit, J., Jones, L., Gomez, A. N., Kaiser, L., and Polosukhin, I. (2017). Attention Is All You Need.
- Wang, J., Liu, Y., and Li, B. (2020). Reinforcement Learning with Perturbed Rewards.
- Yao, P., Wang, H., and Ji, H. (2017). Gaussian mixture model and receding horizon control for multiple UAV search in complex environment. *Nonlinear Dynamics*, 88(2):903–919.
- Yao, P., Zhu, Q., and Zhao, R. (2022). Gaussian Mixture Model and Self-Organizing Map Neural-Network-Based Coverage for Target Search in Curve-Shape Area. *IEEE Transactions on Cybernetics*, 52(5):3971–3983.
- Yue, L., Yang, R., Zhang, Y., Yu, L., and Wang, Z. (2022). Deep Reinforcement Learning for UAV Intelligent Mission Planning. *Complexity*, 2022:e3551508.

Zuluaga, J. G. C., Leidig, J. P., Trefftz, C., and Wolffe, G. (2018). Deep Reinforcement Learning for Autonomous Search and Rescue. In *NAECON 2018 - IEEE National Aerospace and Electronics Conference*, pages 521–524.

Appendix A. Parameters

Table A.7: Simulation parameters used for this work

Parameter	Value	Units
$N_{gaussian}$	4.000	
σ_i	diag(500,500)	
x_{min}, y_{max}	0.000	m
x_{min}, y_{max}	150.000	m
λ	8.000	m
R_{buffer}	2.500	m
$N_{waypoint}$	64.000	
ϵ	0.100	
w_{oob}	1.000	
w_r	0.500	
w_0	0.500	

Table A.8: RAE parameters used for this work

Parameter	Value
Learning rate	1.000E−4
Gradient norm clipping	0.500
L1 regularization coefficient (λ)	1.000E−4
Patience	40.000
Batch size	8.000
# Epochs	5.000E3
# Steps	5.000E4
Optimizer	adam

Table A.9: Reinforcement learning hyperparameters for the various architectures in this work. Default values from Raffin et al. (2021) v2.1.0 were used if not listed in the table.

(a) SAC					
Hyperparam.	Architecture				
	<i>FS_SAC_CONV2D</i>	<i>FS_SAC_FC</i>	<i>FS_SAC_LSTM</i>	<i>LSTMAE_SAC</i>	<i>LSTMAE_SAC</i>
Net width	2.560E2	2.560E2	25.600E1	25.600E1	204.800E1
τ	1.974E-1	1.974E-1	1.974E-1	1.903E-1	1.903E-1
# envs	8.000	8.000	8.000	8.000	8.000
Training freq.	1.000	1.000	1.000	1.000E1	1.000E1
Batch size	1.024E3	1.024E3	1.024E3	5.120E2	5.120E2
Buffer size	5.000E6	5.000E6	5.000E6	5.000E5	5.000E5
Gradient Steps	2.000	2.000	2.000	1.000E2	1.000E2
Learning rate	1.436E-4	1.436E-4	1.436E-4	5.917E-6	5.917E-6
Learning starts	8.092E3	8.092E3	8.092E3	6.547E3	6.547E3
Target entropy	-1.000	-1.000	-1.000	-1.000	-1.000
SDE freq.	5.000	5.000	5.000	4.000	4.000
Optimizer	adam	adam	adam	adam	adam

(b) RPPO		(c) PPO				
Hyperparam.	Architecture	Architecture				
	<i>LSTM_PPO</i>	<i>FS_PPO_CONV2D</i>	<i>FS_PPO_FC</i>	<i>FS_PPO_LSTM</i>	<i>LSTMAE_PPO</i>	
# steps	1.025E4	# steps	6.126E3	5.126E3	6.126E3	3.104E3
# envs	8.000	# envs	8.000	7.000	8.000	8.000
Entropy coef.	2.500E-7	Entropy coef.	2.070E-7	1.070E-7	2.070E-7	1.550E-2
V_f coef.	2.363E-3	V_f coef.	1.356E-2	3.560E-3	1.356E-2	3.287E-1
Batch size	1.280E2	Batch size	2.560E2	1.560E2	2.560E2	6.400E1
Learning rate	8.581E-5	Learning rate	3.108E-4	2.108E-4	3.108E-4	4.360E-4
SDE freq.	2.000	SDE freq.	3.000	2.000	3.000	5.000
# epochs	3.700E1	# epochs	4.000E1	3.000E1	4.000E1	5.800E1
Clip range	1.487E-1	Clip range	1.482E-1	0.482E-1	1.482E-1	8.208E-2
GAE λ	9.749E-1	GAE λ	9.009E-1	8.009E-1	9.009E-1	9.285E-1
Max. grad.	9.896E-1	Max. grad.	1.953E-1	0.953E-1	1.953E-1	6.142E-1
Optimizer	adam	Optimizer	adam	adam	adam	adam